

# Electrochemical modification and surface pre-treatment of boron-doped diamond electrodes with Pd and Pd-Sn nanoparticles for ethanol electrooxidation

Christos K. Mavrokefalos<sup>1</sup>, Maksudul Hasan<sup>1</sup>, Worawut Khunsin<sup>3</sup>, Stefan A. Maier<sup>3</sup>, Richard G. Compton<sup>2</sup>, John S. Foord<sup>1\*</sup>

<sup>1</sup>Department of Chemistry, Chemistry Research Laboratory, University of Oxford, Mansfield Road, Oxford, OX1 3TA, England, UK

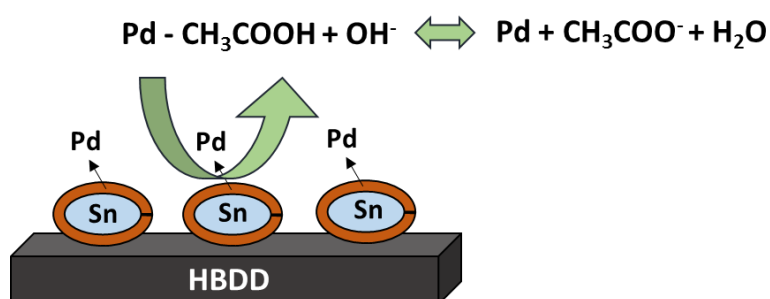
<sup>2</sup>Department of Chemistry, Physical and Theoretical Chemistry Laboratory, University of Oxford, South Parks Road, Oxford, OX1 3QZ, England, UK

<sup>3</sup>Department of Physics, The Blackett Laboratory, Imperial College London, London, SW7 2AZ, England, UK

**Keywords:** diamond, hydrogen termination, electrochemical properties, fuel cells

\*Corresponding author: E-mail: [john.foord@chem.ox.ac.uk](mailto:john.foord@chem.ox.ac.uk) Phone: +44 01865 275967 Fax: +44 01865 275410

The modification of hydrogen terminated boron-doped diamond (HBDD) electrode with pure Pd and Pd-Sn nanoparticles is described in this study. For the synthesis of the two types of HBDD electrode, a potentiostatic and a two-step electrochemical method involving the electrodeposition of Sn; followed by Pd were used, respectively.



The modification of the HBDD electrode with Sn and noble metal Pd by forming shell-core nanoparticles leads to higher electrochemical activity. The electrochemical activity of the shell-core Pd-Sn/HBDD was evaluated towards the electrooxidation of ethanol and compared with that of the Pd/HBDD electrode itself. Higher current densities and less poisoning effects on shell-core Pd-Sn nanoparticles modified HBDD electrode surface during ethanol electrooxidation is seen compared to the Pd itself. Larger poisoning tolerance and improved electrocatalytic activity is observed when the Pd loading is increased. The aforementioned catalysts of this research possessing good stability and efficiency towards ethanol electrooxidation in alkaline media over a long operational time of two hours.

## 1. Introduction

Metal nanoparticle surface modification of carbon substrates constitute common catalysts and have a plethora of benefits<sup>1-5</sup>. Of note are the increase of the oxidation efficiency of alkaline electrolytes compared to the non-functionalised catalyst, the oxidative removal of some poisons and consequently more tolerance as well as the durability of electrocatalyst. Boron-doped diamond (BDD) on the other hand, exhibit unique electrochemical properties in comparison with other carbon materials. The low background current, the high mechanical and electrochemical stability are some of them. Aside from that, resistance to fouling and corrosion in a hostile environment are also notable. Furthermore, it has quite low production cost when grown by chemical vapour deposition (CVD)<sup>6-14</sup>. All the aforementioned properties suggest this material as a promising substrate for supporting the catalysts. Moreover, the modification of diamond electrodes with depositing metal nanoparticles and/or metal oxides<sup>10</sup> as well as metal thin films<sup>15</sup> facilitate the sensitivity towards analytes which cannot be detected on the unmodified surface<sup>16</sup>. In addition, the latter can enhance the selectivity for various electroanalytical applications<sup>17-19</sup>. Boron doped diamond electrodes modified with electrocatalytic metal

nanoparticles have been established widely for their electrochemical applications<sup>6,14,20–26</sup> and increased surface area in the field of adsorptive voltammetry<sup>16,19,27</sup>. One interesting feature also is the fact that diamond electrodes exhibit stable chemical terminations, which can be altered from oxygen to hydrogen chemical termination by putting the electrodes under microwave plasma of hydrogen<sup>28–31</sup>. Foord *et al.* have shown that metal nanoparticles on a hydrogen terminated diamond electrode can differ from those on an oxygen terminated electrode in microstructure<sup>8</sup>. As a result, the hydrogen terminated surface provides stronger electrochemical response and improved physical stability<sup>19</sup>. Nebel *et al.* also have proved that a high concentration of hydrogen functionalities surface can increase conductivity<sup>32</sup>.

In this work, Pd and Pd-Sn modified hydrogen terminated BDD electrodes are proposed for ethanol oxidation of relevance to the direct alkaline fuel cells (DAFC). Diamond has received attracted role recently for fuel cell applications on account of its resistance to electrocorrosion<sup>14,33,34</sup>. Despite the fact that Pt is one of the most active electrocatalyst anodes, it tends to be poisoned by the intermediates of ethanol species such as carbon monoxide (CO)<sup>35</sup>. Consequently, palladium (Pd) seems to be an alternative catalyst, existing more times in earth<sup>36</sup> than Pt and showing more tolerance to carbon monoxide<sup>37</sup>, promising increasing efficiency in the field of alkaline fuel cells<sup>36,38,39</sup>. Regardless of that, Pd can be used in numerous electrochemical applications including pharmaceutical applications<sup>40</sup>, organic synthesis<sup>41,42</sup>, sensing<sup>43</sup> and hydrogen storage<sup>44,45</sup>.

## 2. Experimental section

### 2.1 Chemical reagents

Chemical reagents were purchased from Sigma-Aldrich and used as received without any further purification. These were: palladium (II) chloride (PdCl<sub>2</sub>); and hydrochloric acid (HCl). Tin (II) methanesulfonate 50% aqua solution (C<sub>2</sub>H<sub>6</sub>O<sub>6</sub>S<sub>2</sub>Sn), methanesulfonic acid 70% aqua solution (CH<sub>3</sub>SO<sub>3</sub>H) were purchased from Alfa Aesar. All aqueous solutions were freshly prepared, using milli-Q water (>18 MΩ cm). All the solutions were deaerated using oxygen-free nitrogen gas for a minimum of 20 minutes prior to experiments.

### 2.2 Equipment and experimental set-up

BDD wafers ([B]>10<sup>20</sup> cm<sup>-3</sup>) of 10 x 10 x 0.6 mm were obtained from Element Six Co (UK) and mounted in a home-built PTFE holder with a circular area of 0.38 cm<sup>2</sup> exposed to the electrolyte. The electrochemical measurements were performed with an Autolab PGSTAT 128N potentiostat/galvanostat. The electrochemical depositions were conducted at room temperature (24 ± 1.0°C), using a standard three electrode cell with a Pt counter electrode, a Ag/AgCl and Hg/HgO reference electrodes. The analysis was done with OriginPro 8.5 software (OriginLab Ltd.). The morphology of the deposits was characterised by a Hitachi S530 SEM with a 20 kV acceleration voltage, respectively and the composition of the deposits was measured by XPS using an Al Kα (1486.6 eV) X-ray source. XPS data were curve fitted using CasaXPS software<sup>46</sup>, using a Shirley background<sup>47</sup>. The C 1s peak was calibrated to 285 eV with the following relative sensitivity factors (R.S.F.): C 1s (1.0), O 1s (2.93), Pd 3d (16.0) and Sn 3d (25.1).

### 2.3 Modification of BDD electrodes

Prior to deposition, all BDD electrodes were put in MW-CVD at 600 °C, 45 Torr pressure, 1.5 kW microwave power and H<sub>2</sub> gas flow at 200 sccm for a duration of 45 minutes. At the end of 45 minutes, hydrogen plasma etching was achieved and the samples were cooled down in the MW-CVD by switching off the heating and gradually reducing the microwave power until the plasma disappeared. The samples were cooled down naturally to room temperature. The electrodes were taken out from MW-CVD and examined for hydrogen termination by XPS.

Pd catalyst was then electrodeposited onto HBDD from a deaerated 0.1M HCl solution containing 1mM PdCl<sub>2</sub> by a potentiostatic method. The deposition potential was held at -0.15V (vs Ag/AgCl) until 2.6, 5.2 and 10.4 mC/cm<sup>2</sup> charge passed through the surface. The corresponding metal loading of the aforementioned charges was 1.45, 2.90 and 5.80 µgr/cm<sup>2</sup> respectively. The electrodepositions potential was chosen after cyclic voltammetry on bare diamond wafer in the aforementioned solution, a potential range (-0.1V to -0.4V) in which Pd reduction is occurred<sup>48</sup>.

The second electrode comprised Pd-Sn/HBDD, with Sn being electrodeposited onto HBDD from a deaerated 0.26M C<sub>2</sub>H<sub>6</sub>O<sub>6</sub>S<sub>2</sub>Sn in 1M CH<sub>3</sub>SO<sub>3</sub>H solution through cyclic voltammetry at a potential between -0.6V and +0.5V (vs Ag/AgCl) at 0.01V/s for one cycle. The Sn/HBDD electrode then was removed, rinsed with ultrapure water and dried with N<sub>2</sub>. Pd electrocatalytic particles were electrodeposited onto Sn/HBDD (158 mC/cm<sup>2</sup>: 97 µgr/cm<sup>2</sup>) from a deaerated 0.1M HCl solution containing 1mM PdCl<sub>2</sub>. Again, a potentiostatic method was used in which the potential was held at -0.15V (vs Ag/AgCl) until 2.6, 5.2 and 10.4 mC/cm<sup>2</sup> passed through the electrode surface giving 1.45, 2.90 and 5.80 µgr/cm<sup>2</sup> palladium loading as referred in the previous paragraph.

## 3. Results and Discussions

### 3.1 Morphology, EDX and XPS characterisation of the deposits on HBDD

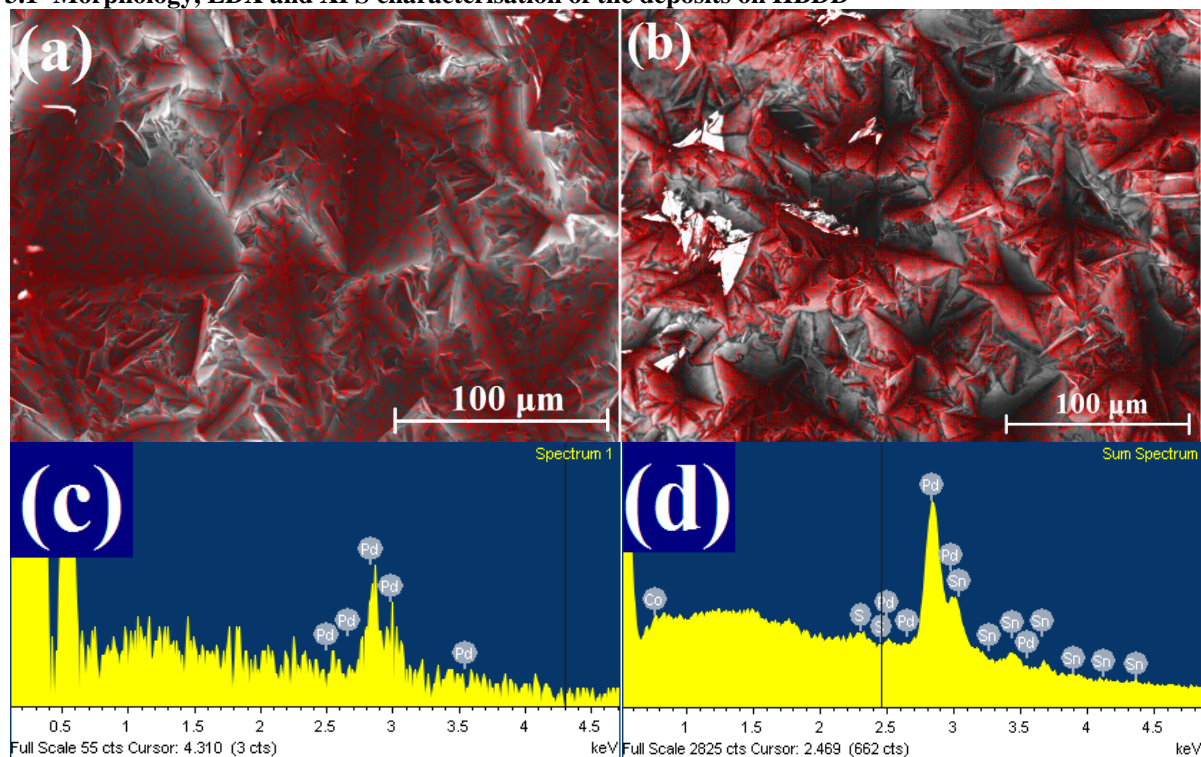


Figure 1 SEM images of (a) Pd deposited on HBDD electrodes and (b) Pd-Sn on HBDD, respectively through chronoamperometry at -0.15V for the Pd and cyclic voltammetry between -0.6V and +0.5V at scan rate of 0.01V/s for the Sn, respectively. EDX spectra of (c) Pd deposited on HBDD electrodes and (d) Pd-Sn on HBDD, respectively.

SEM images of Pd and Pd-Sn after 10.4 mC/cm<sup>2</sup> passage of charge at the potential described in the previous section are shown in Fig. 1 (a-b), respectively. Pd particles in a non-uniform manner are displayed in Fig. 1(a-b). The size of the particles is approximately 10 nm and seems to be uniform throughout the electrode surface at this metal loading. The fact of the non-uniform nature comes from the lateral conductivity of the diamond as well as of the non-uniform distribution of the B dopant as described in previous report<sup>49</sup>. Energy dispersive x-ray spectra provide information for the elemental composition of the electrodes showing quite intense Pd and Pd-Sn peaks (Fig. 1(c) and 1(d), respectively).

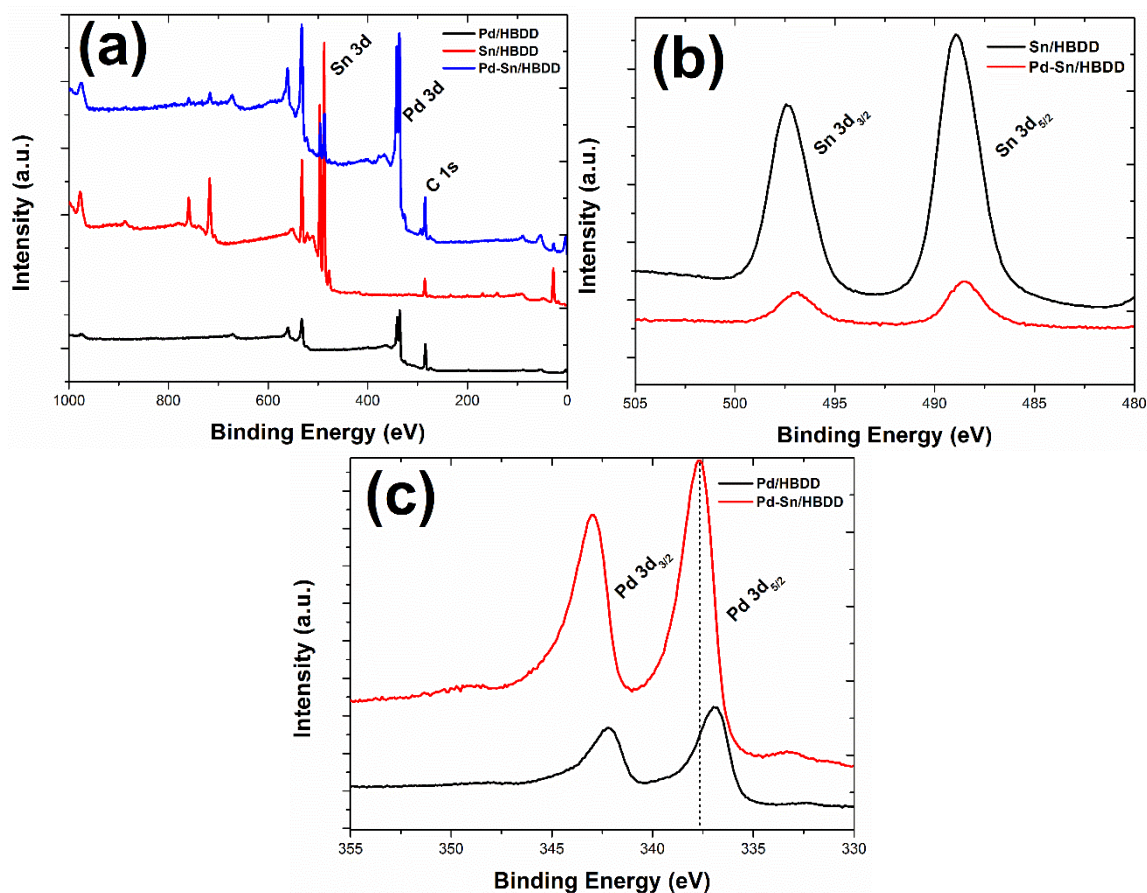


Figure 2 (a) XPS spectra of wide scans of the Sn/HBDD, Pd/HBDD and Pd-Sn/HBDD, respectively. (b) Typical Sn 3d peaks of Sn and Pd-Sn modified HBDD catalysts, respectively. (c) Typical Pd 3d peaks of the Pd and Pd-Sn modified HBDD catalysts, respectively.

XPS was performed in order to investigate the elemental composition of Sn, Pd and Pd-Sn at the diamond interface for the samples in Fig. 2. Figure 2(a) shows the survey scans of the Sn, Pd and Pd-Sn modified HBDDs, respectively. The wide scans indicate that these electrodes contain C, O and the photoelectron peaks of the metal peaks. The Sn modified HBDD has Sn 3d<sub>5/2</sub> and Sn 3d<sub>3/2</sub> peaks at 488 and 497.5 eV respectively<sup>50</sup>. After the modification with Pd, the Sn 3d<sub>5/2</sub> and Sn 3d<sub>3/2</sub> peaks are shifted slightly at 487.5 and 497 eV respectively. Clearly the Sn signal significantly disappeared in the case of the Pd-Sn modified HBDD, fact which indicates that the Sn particles were covered by over layers of Pd. The latter can also be derived by the fact that the intensity of the Sn peak of the Sn/HBDD electrode was initially quite strong and after the modification with Pd this peak was attenuated 5 times. Furthermore, Pd peak has a Pd 3d<sub>5/2</sub> and Pd 3d<sub>3/2</sub> peaks at 338 and 343

eV respectively. The Pd-Sn modified HBDD showed also a tiny shift as seen in Fig. 2c. The Pd 3d<sub>5/2</sub> and Pd 3d<sub>3/2</sub> peaks were shifted at 337 and 342 eV respectively fact which implies some electronic interaction between the two metals and therefore this binding energy shift.

### 3.2 Voltammetric Characterisation

#### 3.2.1 Electrodeposition of the electrocatalysts

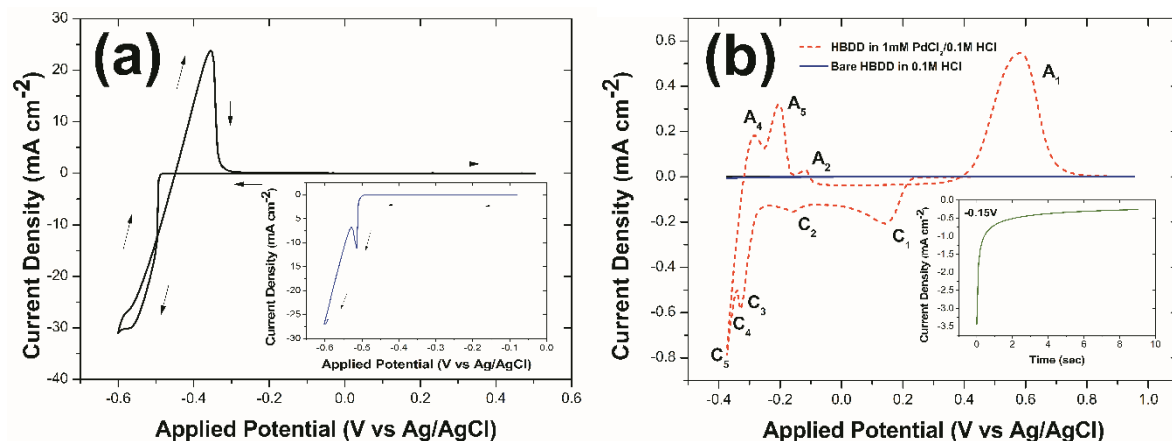


Figure 3 (a) Cyclic voltammogram of bare HBDD in a solution containing 0.26M C<sub>2</sub>H<sub>6</sub>O<sub>6</sub>S<sub>2</sub>Sn in 1M CH<sub>3</sub>SO<sub>3</sub>H at scan rate of 0.01V/s (inset: linear sweep voltammogram of bare HBDD in 0.26M C<sub>2</sub>H<sub>6</sub>O<sub>6</sub>S<sub>2</sub>Sn in 1M CH<sub>3</sub>SO<sub>3</sub>H). (b) Cyclic voltammogram of bare HBDD in a solution containing 0.1M HCl and 1mM PdCl<sub>2</sub>/0.1M HCl respectively at scan rate of 0.01 V/s (inset: chronoamperogram of Pd deposition in 1mM PdCl<sub>2</sub>/0.1M HCl on bare HBDD at constant potential of -0.15V).

A typical cyclic voltammogram of bare HBDD in a solution containing 0.26M C<sub>2</sub>H<sub>6</sub>O<sub>6</sub>S<sub>2</sub>Sn in 1M CH<sub>3</sub>SO<sub>3</sub>H is shown in Fig. 3(a). The Sn is deposited in the cathodic scan in potential range of -0.49V and -0.6V and stripped out in the anodic scan with a sharp peak at potential -0.35V. A pronounced nucleation loop in the cathodic scan indicates that Sn deposition on HBDD surface occurred through the formation of small nuclei followed by further growth. A typical voltammogram of bare HBDD in a solution containing 1mM PdCl<sub>2</sub>/0.1M HCl is also illustrated in Fig. 3(b). The Pd is deposited in the forward scan in potential range of +0.22V and -0.37V. Cathodic current peaked initially at 0.15V (peak C<sub>1</sub>) and stayed steady until reached the sufficient overpotential value at -0.25V and then increased sharply to maximum at -0.33V (peak C<sub>3</sub>) near the diffusion limited reduction of Pd ions, which then decreased beyond this peak as the mass transfer became diffusion dominant, reached minimum at -0.34V (peak C<sub>4</sub>) followed by an increase due to bulk H<sub>2</sub> evolution (peak C<sub>5</sub>). The potential region of 0.22-0.15V is completely represents the Pd metal deposition without hydrogen underpotential deposition (H<sub>UPD</sub>), and after this point i.e., in the cathodic range between -0.15V and -0.37V deposition occurs simultaneously with H<sub>UPD</sub> onto the freshly deposited Pd, in which peaks A<sub>2</sub>, A<sub>4</sub>, A<sub>5</sub>) are due to the H desorption process. The A<sub>1</sub>/C<sub>1</sub> peaks show the Pd stripping from the electrode surface having a maximum peak at +0.58V and the reduction of it with a peak at +0.14V in the anodic and cathodic scan respectively.

### 3.2.2 Electrochemical activity of the electrocatalysts

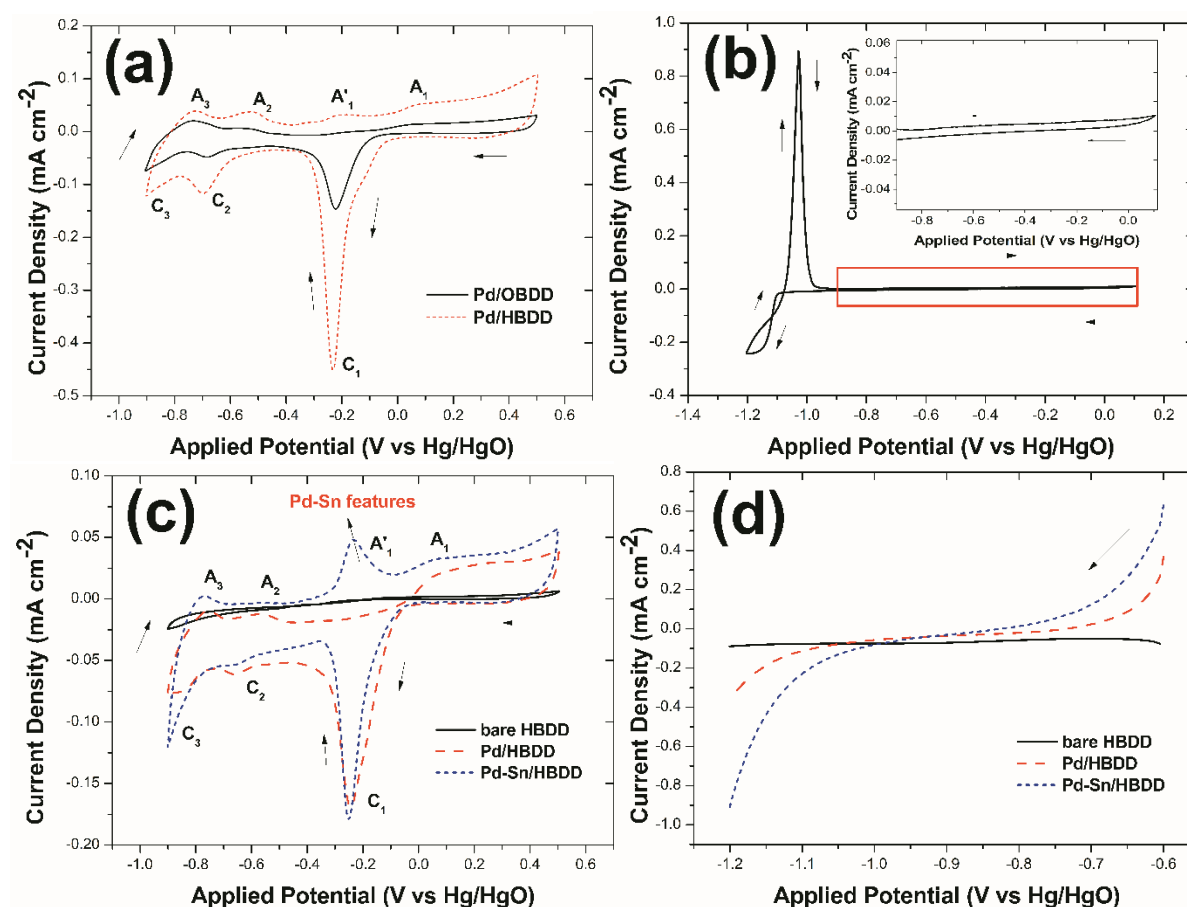


Figure 4 Cyclic voltammogram of (a) Pd/OBDD and Pd/HBDD ( $5.80 \mu\text{gr}/\text{cm}^2$ ), (b) Sn/HBDD ( $97 \mu\text{gr}/\text{cm}^2$ ), (c) Pd and Pd-Sn modified HBDD ( $2.90 \mu\text{gr}/\text{cm}^2$ ), and (d) Linear sweep voltammograms of the Pd and Pd-Sn modified HBDD ( $2.90 \mu\text{gr}/\text{cm}^2$ ), respectively in  $0.5\text{M}$  KOH solution at scan rate of  $0.02 \text{ V/s}$  (all CVs were started from open circuit potential).

The electrochemical activity of the electrocatalysts was characterised by cyclic voltammetry in  $0.5\text{M}$  KOH. The behaviour of Pd nanoparticles on fairly oxidised surface and on hydrogen terminated surface was compared initially (Figure 4a). In Fig. 4(a) we observe various features for examples, (i) Pd oxidation and reduction peaks ( $A_1/C_1$ ) at  $+0.05\text{V}$  and  $-0.23\text{V}$  respectively; It can be attributed to the formation of a palladium oxide layer on the surface of the catalyst. However, the exact mechanism of the Pd oxidation remains unclear<sup>51</sup>. It has been generally accepted that  $\text{OH}^-$  ions are first chemisorbed in the initial stage of the oxide formation and then they transformed into higher valence oxides at higher potentials, as reported in literature<sup>52–54</sup>. (ii) Hydrogen adsorption and desorption peaks of Pd surface at  $-0.65\text{V}$  and  $-0.9\text{V}$  ( $C_2$ ,  $C_3$  and  $A_3$ ). And (iii) a prepeak ( $A'_1$ ) appeared at  $-0.2 \text{ V}$  in the anodic scan before the main Pd surface oxidation process start, which corresponds to oxidation at favourable sites on the palladium surface<sup>55</sup>. The corresponding oxide reduction peak for  $A_1$  may appear at limited potential scanning towards incomplete oxidation and reduction (peak  $A_1/C_1$ ) of the Pd surface as described in elsewhere<sup>55</sup>. However, the hydrogen terminated Pd/HBDD electrode showed higher current densities and ability to adsorb hydrogen ions than that of the oxygen terminated Pd/BDD electrode. This is likely to arise from the fact that there is a high concentration of hydrogen functionalities on the surface and the overall conductivity is increased according to previous report<sup>32</sup>. Hence, our interest was focused on the hydrogen terminated BDD surfaces as electrode and modification of the electrode by electrochemically deposited shell-core Pd-Sn nanoparticles towards electrooxidation of ethanol (see Figure 5). The cyclic voltammogram of

Sn/HBDD (Fig. 4(b)) does not show electrochemical activity in potential range of -0.9V to +0.1V and thus, Sn is inactive on own within the electrochemical window where Pd is electrocatalytically active. However, a cathodic peak at potential more negative than -1.1V and an anodic peak at -1.02V in the reverse scan are seen, which is due to deposition and dissolution of unknown electroactive species onto Sn surface. The cyclic voltammogram of 5.2 mC/cm<sup>2</sup> passage of charge (2.90  $\mu$ gr/cm<sup>2</sup>) of the Pd onto HBDD and Sn/HBDD electrode are illustrated in Fig. 4(c). Various features as the ones observed for the Pd/OBDD and Pd/HBDD catalysts are distinguished at the same potential range. However, of note is the feature at -0.22V in the reverse (anodic) scan which only occur in the Pd-Sn modified HBDD and are not seen at its Pd, bare HBDD or Sn modified counterparts<sup>56–58</sup> (see also Fig. 4(b)). The aforementioned features are consistent with the Sn particles serving as reactive centres for the subsequent deposition of Pd, such that the resultant Pd-Sn nanoparticles seem to have core-shell structures. The modification of the HBDD electrode with transition metal Sn and noble metal Pd by forming shell-core nanoparticles leads to higher currents and more hydrogen adsorption. Regarding the hydrogen evolution, more evidence is provided from the linear sweep voltammogram in Fig. 4(d). The hydrogen evolution on Pd-Sn/HBDD surface occurs in cathodic scan at the potential of -1.0V, the onset potential is much lower when Pd interacts with the underlying Sn compare to Pd/HBDD electrode alone in which hydrogen evolution occurs at -1.07V. This result evidenced that a thin layer of Pd has been formed on top of the Sn helping the electronic interaction between the two metals.

The metal coverage of Pd can be estimated from the charge obtained from the area under the voltammogram applying Faraday's Law. Determining the ratio of the charge required for desorption of an oxygen monolayer on the Pd (111) surface<sup>59</sup> (0.424 mC cm<sup>-2</sup>) to that of  $Q_o$  which is the coulombic charge of the oxygen desorption on the Pd surface, the electroactive surface area (EAS) of the pure Pd electrocatalyst can be also estimated. In addition, the specific surface area (SSA) can be defined as the electroactive surface area divided by the metal loading. All the above information is included in the Table 1.

The electroactive as well as the specific surface areas are almost the same for the two catalysts. The particles size is also approximately the same, which is verified by the SEM images. The difference between the Pd/HBDD and the bimetallic catalyst is roughly 1.5 nm which cannot be observed from the SEM images though.

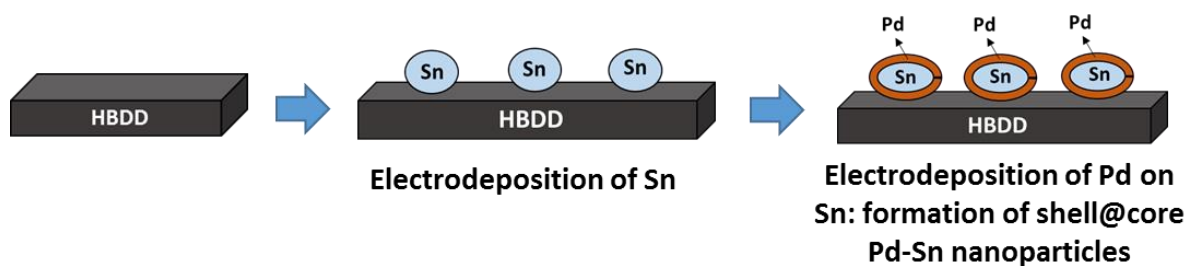


Figure 5 Schematic representation of the electrodeposition of Sn and subsequent electrodeposition of Pd on Sn nanoparticles for the formation of shell-core Pd-Sn nanostructures.

### 3.3 Evaluation of Pd-Sn electrocatalysts preparation conditions on ethanol oxidation characteristics

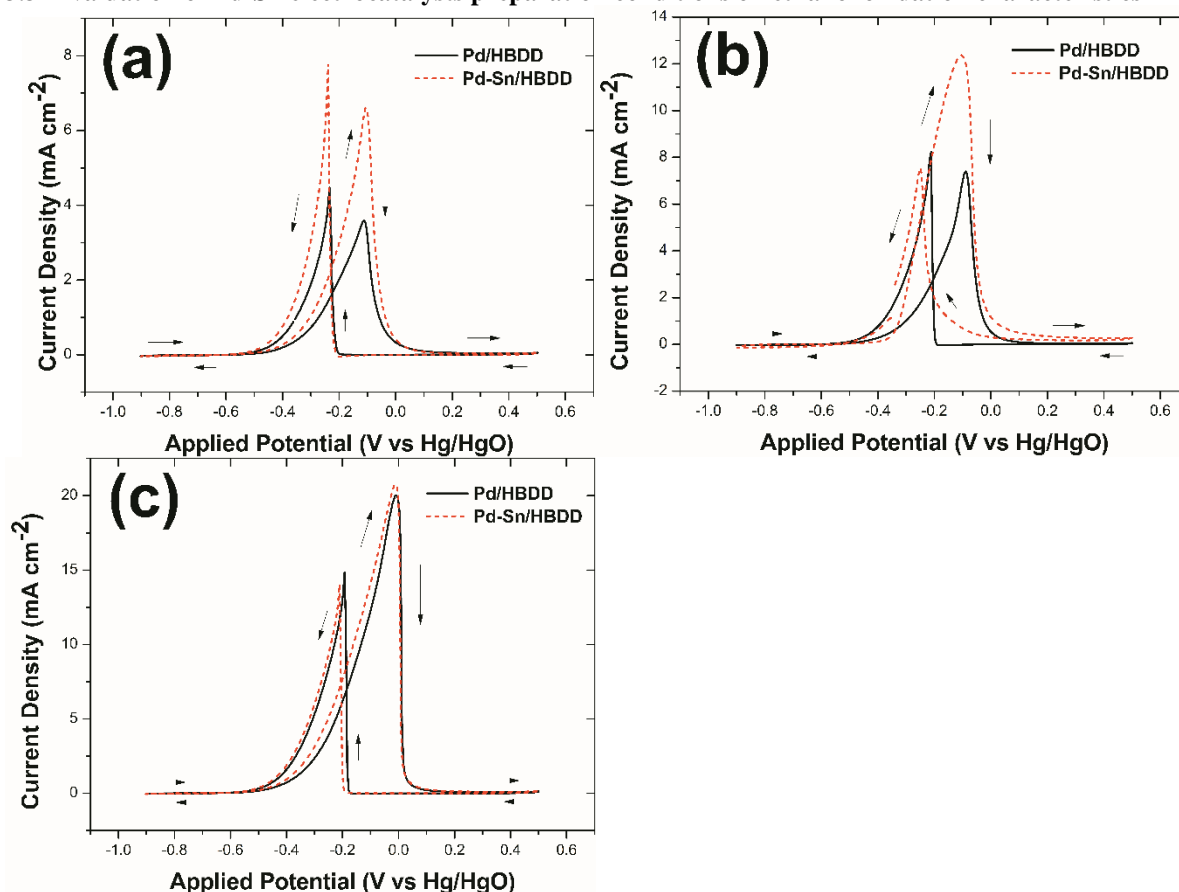


Figure 6 (a, b) Cyclic voltammograms of Pd and Pd-Sn modified HBDD with 1.45  $\mu\text{gr}/\text{cm}^2$  (i.e., 2.6  $\text{mC}/\text{cm}^2$  charge) and 2.90  $\mu\text{gr}/\text{cm}^2$  (i.e., 5.2  $\text{mC}/\text{cm}^2$  charge) Pd loading, respectively in 0.5M KOH and 1M EtOH at scan rate of 0.02 V/s. (c) Cyclic voltammograms of Pd and Pd-Sn modified HBDD (with 5.80  $\mu\text{gr}/\text{cm}^2$ : Pd loading) in 0.5M KOH and 1M EtOH at scan rate of 0.02 V/s. (all CVs were started from open circuit potential). Cyclic voltammograms shown here are steady state taken after 10 cycles.

The electrocatalytic activity of the Pd/HBDD and Pd-Sn/HBDD towards the oxidation of ethanol was evaluated through cyclic voltammetry. The modified electrodes were placed in solutions containing 0.5M KOH and 1M EtOH and cyclic voltammograms were obtained. The results are shown in Fig. 6(a) and 6(b). The onset potential for electrooxidation of ethanol is observed at -0.5V, no current response before -0.5V, which implies that the electrode is inactive before this overpotential. A considerable amount of current passed through as the potential scanned positively (anodic) higher than the respective onset electrooxidation potential and the peak current at around -0.1V, -0.12V and -0.02V were due to the ethanol oxidation onto electrodes Pd/HBDD (1.45 $\mu\text{gr}/\text{cm}^2$ ), Pd-Sn/HBDD (2.90  $\mu\text{gr}/\text{cm}^2$ ), and Pd-Sn/HBDD (5.80  $\mu\text{gr}/\text{cm}^2$ ), respectively, as shown in Fig 6. However, the peak position is slightly shifted as the Pd loading increased, which is due to the electronic interaction of the Pd in outer shell of the nanoparticles with metallic Sn in the core. The peak in the forward scan refers to the oxidation of the fresh ethanol species accumulated on the surface. All electrodes are deactivated at the same potential around +0.1V and reactivated again in the reverse scan (cathodic) at -0.18V giving a second oxidation wave at around -0.24V<sup>56,58</sup>. The second peak implies the oxidation of the incomplete carbonaceous species of the ethanol. Previous studies suggested that the reduced current at more positive potentials was related to the formation of a Pd oxide layer on the surface of the electrode at higher potentials<sup>52,60-62</sup>. The formation of the oxide layer can block the adsorption of the reactive species onto the Pd

surface and lead to a decrease in the electrocatalytic activity. As long as positive going sweep proceeds more Pd oxide covers the surface of the electrode and therefore the current of the oxidation of ethanol is further dwindled<sup>51</sup>. The overall electrode resistance to poisoning by the incomplete oxidation of the adsorbed carbonaceous species ( $\text{CH}_3\text{CO}_{\text{ads}}$ ) of the ethanol is correlated to the ratio of the forward oxidation current peak ( $I_f$ ) and the backward oxidation current peak ( $I_b$ )<sup>63,64</sup>. In Fig. 6(a), Pd-Sn modified HBDD with the lowest amount of Pd (2.6 mC/cm<sup>2</sup> charge i.e., 1.45  $\mu\text{gr}/\text{cm}^2$ ), gives higher current responses compare to the Pd/HBDD electrode but the resistance to poisoning is relatively low (see also Table 1). The tolerance ratio towards the ethanol is getting larger when the amount of Pd is increased as it is shown in Fig. 6(b) and 6(c). Conversely, the Pd-Sn/HBDD with the higher Pd loading in Fig. 6(b) (2.90  $\mu\text{gr}/\text{cm}^2$ ) not only showed higher current densities in comparison with Pd/HBDD itself but also the resistance of the electrode to poisoning by the absorbed ethanol species was higher. To be more precise, the tolerance ratio of the Pd-Sn/HBDD with 2.90  $\mu\text{gr}/\text{cm}^2$  loading seems to have its highest value ( $I_f/I_b=1.63$ ) at this specific loading which is higher not only from the Pd/HBDD of the same metal loading ( $I_f/I_b=0.89$ ) but also of the one which has the double amount of palladium ( $I_f/I_b=1.35$ ). Furthermore, there was a slight shift in the potential from -0.1V to -0.12V for the Pd modified HBDD and the Pd-Sn/HBDD, respectively.

On the other hand, when the loading of the catalyst increased twice the current responses of both Pd/HBDD and Pd-Sn/HBDD were almost the same (Fig 6(c)). That means that the electronic interaction between the two metals started to be disappeared because thicker overlayers shell of Pd onto the inner Sn metal nanoparticles. Consequently, the threshold of Pd loading and therefore the better ratio of resistance to poisoning by the adsorbed ethanol pieces was 2.90  $\mu\text{gr}/\text{cm}^2$  (5.2 mC/cm<sup>2</sup> passage of charge).

Stability tests up to 1 hour and 40 minutes voltammetry in the ethanol solution showed good stability. Despite a small initial current drop during the first scans, Pd and Pd-Sn nanoparticles are bonded in a stable fashion on the hydrogen terminated surface.

Experiments were conducted also on Sn electrodes with 15 times more Pd on it and the result showed that there is no interaction between the two metals. Clearly, a huge overlayer of Pd was created onto the surface of Sn nanoparticles and therefore, the current was increased but it was not higher than the Pd itself. In addition the tolerance towards the ethanol oxidation was reduced due to that big overlayer of Pd, hiding the electronic properties of the two metals as well as the properties and extra conductivity from the hydrogen termination. An overall picture of the mechanism of ethanol oxidation reaction and at the same time the role of various Pd loading towards the latter oxidation reaction is illustrated in Figure 7.

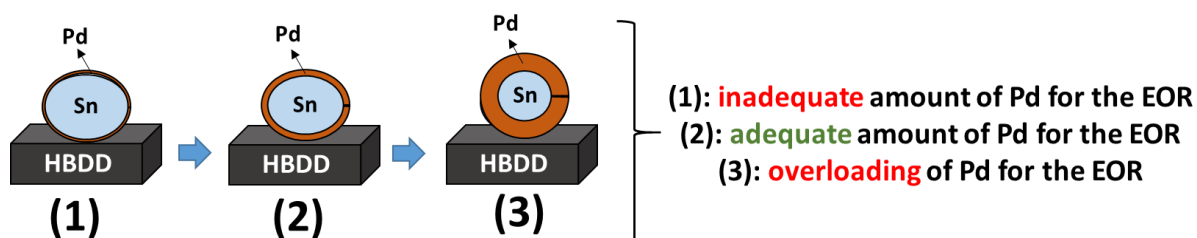


Figure 7 Representation of mechanism of Ethanol Oxidation Reaction (EOR) on various Pd loadings of shell-core Pd-Sn nanostructures.

Table 1 Pd features after electrodeposition through chronoamperometry.

a/a	Electrodes	Charge (mC/cm <sup>2</sup> )	Pd loading (μgr/cm <sup>2</sup> )	O des. charge (mC/cm <sup>2</sup> )	Electroactive surface area, EAS (cm <sup>2</sup> /cm <sup>2</sup> )	Specific surface area, SSA (m <sup>2</sup> /gr)	Mass activity (mA/gr) x 10 <sup>6</sup>	Particles size (nm)	Forward current peak (I <sub>f</sub> ) of ethanol electrooxidation (mA/cm <sup>2</sup> )	I <sub>f</sub> /I <sub>b</sub>
<b>1</b>	Pd/HBDD	2.6	1.45	0.71	1.67	115.17	2.48	4.33	3.60	0.81
	Pd-Sn/HBDD			0.81	1.92	132.41	4.56	3.77	6.61	0.86
<b>2</b>	Pd/HBDD	5.2	2.90	0.71	1.67	57.59	2.55	8.66	<b>7.39</b>	<b>0.89</b>
	Pd-Sn/HBDD			0.74	1.74	60.00	4.26	8.32	<b>12.37</b>	<b>1.63</b>
<b>3</b>	Pd/HBDD	10.5	5.8	1.81	4.28	73.79	3.45	6.76	20.02	1.35
	Pd-Sn/HBDD			1.66	3.91	67.41	3.58	7.40	20.78	1.49

### 3.4 Tafel analysis

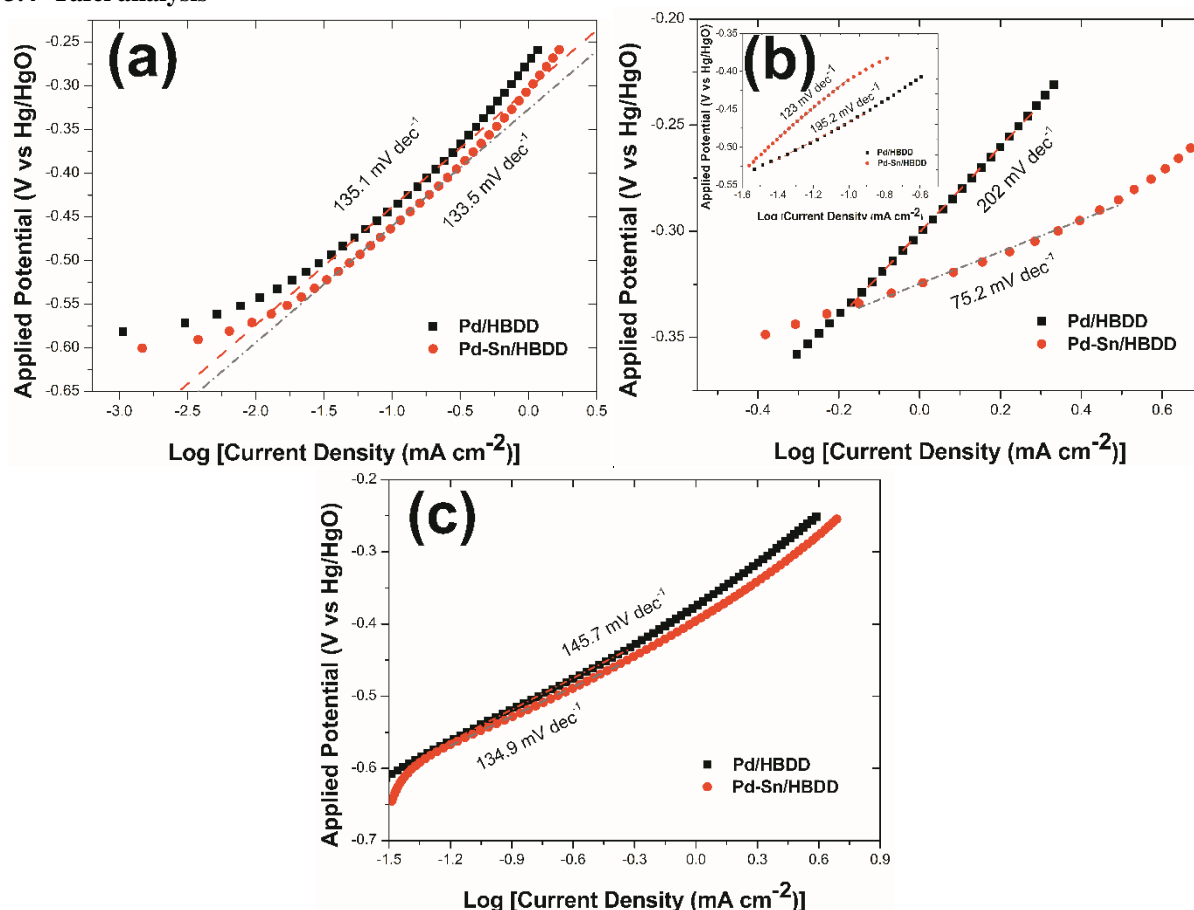


Figure 8 Tafel plots of anodic polarisation curve for ethanol oxidation in 0.5M KOH and 1M EtOH: (a, b) of Pd and Pd-Sn modified HBDD with 1.45 μgr/cm<sup>2</sup> (i.e., 2.6 mC/cm<sup>2</sup>) and 2.90 μgr/cm<sup>2</sup> (i.e., 5.2 mC/cm<sup>2</sup>) Pd loading, respectively. Inset of 6b: different potential range of Pd and Pd-Sn modified HBDD with 2.90 μgr/cm<sup>2</sup> (i.e., 5.8 mC/cm<sup>2</sup>) Pd loading. (c) of Pd and Pd-Sn modified HBDD (with 5.80 μgr/cm<sup>2</sup>: Pd loading).

The electrochemical activity of Pd and Pd-Sn modified HBDD electrodes was investigated further by measuring the anodic polarisation curve and calculating kinetic parameters from Tafel plots as shown in Fig. 6. The Tafel plots are calculated from the steady state cyclic voltammograms shown in Fig. 5. In Fig. 6(a), slopes in the lower onset potential region, namely charge transfer control region, are approximately the same for the both electrodes, which are 135.1 and 133.5 mV dec<sup>-1</sup> for Pd/HBDD and Pd-Sn/HBDD respectively with the lower amount of Pd loading (1.45 μgr/cm<sup>2</sup>). The Tafel slope indicates that the kinetics of ethanol oxidation reaction in the lower potential region of -0.6V to -0.25V is dominated by the adsorption of hydroxyl ions on the Pd surface<sup>51</sup>. Nevertheless, the small deviation in the Tafel slope between the Pd/HBDD and Pd-Sn/HBDD shows that the kinetics of the ethanol oxidation reaction is not only controlled by the adsorption of hydroxyl by it also

altered by other surface reactions e.g. oxide layer that is formed on the surface of the Pd as reported in section 3.2. The same description can be attributed for the Fig. 6(b) with  $2.90 \mu\text{gr}/\text{cm}^2$  Pd loading catalysts. Each plot has been fitted to one linear region. The Tafel slope for Pd/HBDD ( $195.2 \text{ mV dec}^{-1}$ ) is higher than that of Pd-Sn/HBDD ( $123 \text{ mV dec}^{-1}$ ) in the lower potential indicating the adsorption of higher hydroxyl ( $\text{OH}_{\text{ads}}$ ) ions on the surface of the shell-core Pd-Sn nanoparticles. The lowest value obtained for Pd-Sn/HBDD indicates a higher charge transfer rate during the electrooxidation of ethanol by comparison with the Pd/HBDD electrode itself. Similarly, Pd-Sn/HBDD electrode showed lower slope ( $75.2 \text{ mV dec}^{-1}$ ) in a slightly higher potential region -0.35 to -0.25 (above the charge transfer control region) in comparison with Pd/HBDD electrode ( $202 \text{ mV dec}^{-1}$ ) (see Fig. 6(b)). The lowest value indicates the higher charge transfer during the ethanol electrooxidation on Pd-Sn/HBDD electrode compare to the counterpart Pd/HBDD. The fact of which is probably due to underneath Ni core structure, which suppress the formation of the inactive oxide layer in the potential higher than -0.35V. In Fig. 6(c), Tafel plot of the Pd/HBDD and Pd-Sn/HBDD with further increased in Pd loading ( $5.80 \mu\text{gr}/\text{cm}^2$ ) is illustrated. The slopes slightly differ from each other in the charge transfer control region, which are  $145.7 \text{ mV dec}^{-1}$  and  $134.9 \text{ mV dec}^{-1}$  for the former and the latter, respectively. The Tafel slopes are similar for all electrodes and good agreement with the Temkin-type adsorption for hydroxyl ( $\text{OH}_{\text{ads}}$ ) and acyl ( $\text{CH}_3\text{CO}_{\text{ads}}$ ) ions at lower potential region (-0.6V to -0.4V) indicating the similarity of reaction mechanism for ethanol electrooxidation<sup>51</sup>.

### 3.5 Amperometric response of the catalysts in ethanol

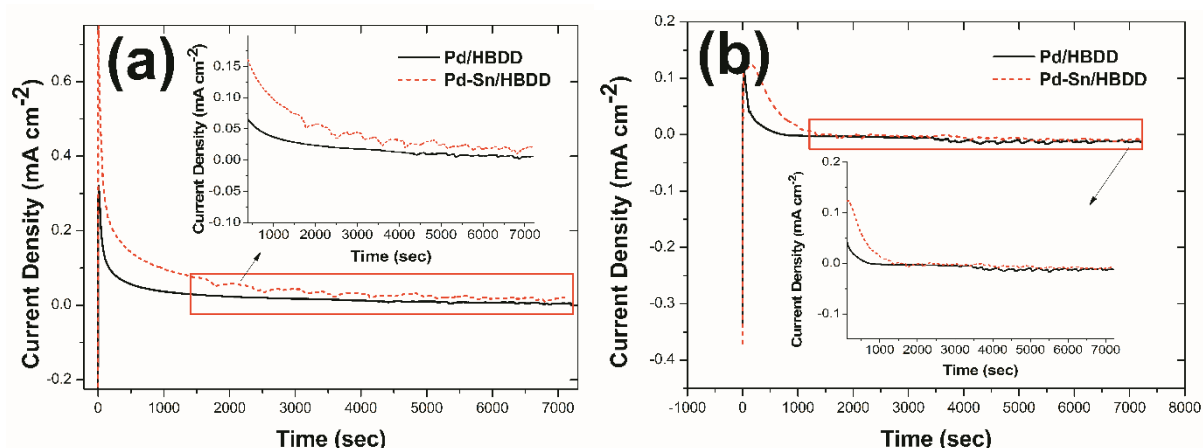


Figure 9 (a, b) Chronoamperometric response of Pd and Pd-Sn modified HBDD after  $2.6 \text{ mC}/\text{cm}^2$  and  $5.2 \text{ mC}/\text{cm}^2$  passage of charge respectively in  $0.5\text{M KOH}$  and  $1\text{M EtOH}$  at potential -0.15 V.

Chronoamperometry was performed to investigate the stability of Pd-Sn/HBDD electrocatalysts towards ethanol oxidation and the obtained result is compared with that of Pd/HBDD as demonstrated in Fig. 9. The electrodes were held at fixed potential -0.15V and run for 7200 seconds. The current density decayed sharply for the Pd/HBDD but is more gradual for the Pd-Sn/HBDD electrocatalyst. Current densities remain stable for much of this period and finally the results are in consistence with the performance of the cyclic voltammetry as described in the previous section (section 3.3). To be more precise, the Pd-Sn/HBDD showed the highest current response in relationship with the Pd itself. The decrease current with the increase in time is attributed to the combined effects of electrocatalyst poisoning by the chemisorbed carbonaceous oxidative intermediates and the concentration polarisation with time (i.e., limited mass transport with increasing reaction time).

#### 4. Conclusions

The hydrogen terminated boron doped diamond (HBDD) electrode was modified with Pd and Pd-Sn nanoparticles by electrochemical techniques. A potentiostatic electrochemical deposition method was used to deposit noble metal Pd and transition metal Sn as nanoparticles onto HBDD towards investigation of the electrocatalytic properties. XPS and electrochemical experiments suggest that Pd can be deposited on the Sn in order to form shell-core nanoparticles where the size of the particles is almost the same regardless of the catalyst's composition (monometallic or bimetallic). The modification of the HBDD electrode with Sn and Pd by forming shell-core nanoparticles leads to higher electrochemical activity. Ethanol oxidation on shell-core Pd-Sn/HBDD electrodes occurs at higher current densities and with less electrode poisoning than the Pd/HBDD itself. This phenomenon is attributed to better dispersion of the Sn nanoparticles on the hydrogen terminated electrode surface and consequently electronic properties are altered in the bimetallic interface as well as in the reaction interface owing to thin shell-core nanoarchitecture. Hence, Pd loading found to be important mostly due to the aforementioned reason. Lower amounts of palladium form a thin overlayer on top of the Sn nanoparticles allows the electronic interaction between them while the higher amounts of Pd loading do not facilitate such interface interaction between the two metals. Finally, the shell-core Pd-Sn/HBDD catalyst shows higher stability towards ethanol oxidation over a long period of time in comparison with the Pd/HBDD alone. The proper tuning of the Pd shell thickness on a second transition metal along with the surface termination effects of the boron doped diamond electrode plays a crucial role in achieving the high mass and specific electrocatalytic activity of Pd towards ethanol electrooxidation.

#### Acknowledgment

Authors acknowledge Marie Curie Actions co-funded Irish Research Council Elevate fellowship ELEVATEPD/2014/15.

#### Notes

The authors declare no competing financial interest.

#### References

1. Cunha EM, Ribeiro J, Kokoh KB, De Andrade a. R. Preparation, characterization and application of Pt-Ru-Sn/C trimetallic electrocatalysts for ethanol oxidation in direct fuel cell. *Int J Hydrogen Energy*. 2011;36(17):11034–11042. doi:10.1016/j.ijhydene.2011.06.011.
2. Hsu RS, Higgins D, Chen Z. Tin-oxide-coated single-walled carbon nanotube bundles supporting platinum electrocatalysts for direct ethanol fuel cells. *Nanotechnology*. 2010;21:165705. doi:10.1088/0957-4484/21/16/165705.
3. Loukrakpam R, Brankovic SR, Strasser P. A Study of Au/C Nanoparticles with Pt Monolayer and Sub-Monolayer Electrocatalysts for Ethanol Oxidation Reaction. *ECS Trans*. 2013;58(1):1733–1736. doi:10.1149/05801.1733ecst.
4. Gacutan EM, Climaco MI, Telan GJ, Malijan F, Hsu HY, Garcia J, Fulo H, Tongol BJ Nanostructured carbon-supported Pd electrocatalysts for ethanol oxidation: synthesis and characterization. *Adv Nat Sci Nanosci Nanotechnol*. 2012;3:045016. doi:10.1088/2043-6262/3/4/045016.
5. Kepeniene V, Tamasauskaite-Tamasiunaite L, Jablonskiene J, Vaiciuniene J, Kondrotas R., Juskenas R, Norkus E. Investigation of Graphene Supported Platinum-Cobalt Nanocomposites as Electrocatalysts for Ethanol Oxidation. *J Electrochem Soc*. 2014;161(14):F1354–F1359. doi:10.1149/2.0511414jes.

6. Rao TN, Fujishima A. Recent advances in electrochemistry of diamond. *Diam Relat Mater.* 2000;9(3-6):384–389. doi:10.1016/S0925-9635(99)00234-4.
7. Swain GM. *Thin-Film Diamond II*. Elsevier; (Elsevier, San Diego, 2004), pp. 121-148. doi:10.1016/S0080-8784(04)80016-4.
8. Shpilevaya I, Smirnov W, Hirsz S, Yang N, Nebel CE, Foord JS. Nanostructured diamond decorated with Pt particles: preparation and electrochemistry. *RSC Adv.* 2014;4(2):531. doi:10.1039/c3ra43763a.
9. Chen L, Hu J, Foord JS. Electrodeposition of a Pt-PrO  $2-x$  electrocatalyst on diamond electrodes for the oxidation of methanol. *Phys Status Solidi.* 2012;209(9):1792–1796. doi:10.1002/pssa.201200049.
10. Kraft A, Doped Diamond : A Compact Review on a New , Versatile Electrode Material. 2007;2:355–385.
11. Lu X, Hu J, Foord JS, Wang Q. Electrochemical deposition of Pt–Ru on diamond electrodes for the electrooxidation of methanol. *J Electroanal Chem.* 2011;654(1-2):38–43. doi:10.1016/j.jelechem.2011.01.034.
12. McCreery RL. Advanced carbon electrode materials for molecular electrochemistry. *Chem Rev.* 2008;108(7):2646–87. doi:10.1021/cr068076m.
13. Toghiani KE, Compton RG. Electrochemical Non-enzymatic Glucose Sensors : A Perspective and an Evaluation. *Int. J. Electrochem. Sci.* 2010;5:1246–1301.
14. Compton RG, Foord JS, Marken F. Electroanalysis at Diamond-Like and Doped-Diamond Electrodes. *Electroanalysis.* 2003;15(17):1349–1363. doi:10.1002/elan.200302830.
15. Chatterjee A, Foord J. Electrochemical deposition of nanocrystalline zinc oxide at conductive diamond electrodes. *Diam Relat Mater.* 2006;15(4-8):664–667. doi:10.1016/j.diamond.2005.11.007.
16. Toghiani KE, Compton RG. Metal Nanoparticle Modified Boron Doped Diamond Electrodes for Use in Electroanalysis. *Electroanalysis.* 2010;22(17-18):1947–1956. doi:10.1002/elan.201000072.
17. Lourenço AS, Sanches F a C, Magalhães RR, et al. Electrochemical oxidation and electroanalytical determination of xylitol at a boron-doped diamond electrode. *Talanta.* 2014;119:509–516. doi:10.1016/j.talanta.2013.11.030.
18. Mansano GR, Eisele APP, Dall’Antonia LH, Afonso S, Sartori ER. Electroanalytical application of a boron-doped diamond electrode: Improving the simultaneous voltammetric determination of amlodipine and valsartan in urine and combined dosage forms. *J Electroanal Chem.* 2015;738:188–194. doi:10.1016/j.jelechem.2014.11.034.
19. Shpilevaya I, Foord JS. Electrochemistry of Methyl Viologen and Anthraquinonedisulfonate at Diamond and Diamond Powder Electrodes: The Influence of Surface Chemistry. *Electroanalysis.* 2014;26(10):2088–2099. doi:10.1002/elan.201400310.
20. Panizza M, Cerisola G. Application of diamond electrodes to electrochemical processes. *Electrochim Acta.* 2005;51(2):191–199. doi:10.1016/j.electacta.2005.04.023.

21. Swain GM, Anderson AB, Angus JC. Applications of Diamond Thin Films in Electrochemistry. *MRS Bull.* 1998;23:56-60.
22. Wei M, Terashima C, Lv M, Fujishima A, Gu Z-Z. Boron-doped diamond nanograss array for electrochemical sensors. *Chem Commun (Camb).* 2009;(24):3624–6. doi:10.1039/b903284c.
23. Lv M, Wei M, Rong F, Terashima C, Fujishima A, Gu Z-Z. Electrochemical Detection of Catechol Based on As-Grown and Nanograss Array Boron-Doped Diamond Electrodes. *Electroanalysis.* 2010;22(2):199–203. doi:10.1002/elan.200900296.
24. Szunerits S, Coffinier Y, Galopin E, Brenner J, Boukherroub R. Preparation of boron-doped diamond nanowires and their application for sensitive electrochemical detection of tryptophan. *Electrochem commun.* 2010;12(3):438–441. doi:10.1016/j.elecom.2010.01.014.
25. Biosensing AG. Fabrication of Boron-Doped Diamond Nanorod Forest Electrodes and Their. 2009;3(8):2121–2128.
26. Antonio M, Alfaro Q, Ferro S, Martínez-huitle CA, Vong YM. Boron Doped Diamond Electrode for the Wastewater Treatment. 2006;17(2):227–236.
27. Gan P, Foord JS, Compton RG. Ionic Liquid-Carbon Nanotube Modified Screen-Printed Electrodes and Their Potential for Adsorptive Stripping Voltammetry. 2014;44(0):1886–1892. doi:10.1002/elan.201400214.
28. Nebel CE, Yang N, Uetsuka H, Osawa E, Tokuda N, Williams O. Diamond nano-wires, a new approach towards next generation electrochemical gene sensor platforms. *Diam Relat Mater.* 2009;18(5-8):910–917. doi:10.1016/j.diamond.2008.11.024.
29. Mehedi H, Hebert C, Ruffinatto S, Eon D, Omnes F, Gheeraert E. Formation of oriented nanostructures in diamond using metallic nanoparticles. *Nanotechnology.* 2012;23:455302. doi:10.1088/0957-4484/23/45/455302.
30. Kriele A, Williams O a., Wolfer M, Hees JJ, Smirnov W, Nebel CE. Formation of nano-pores in nanocrystalline diamond films. *Chem Phys Lett.* 2011;507(4-6):253–259. doi:10.1016/j.cplett.2011.03.089.
31. Smirnov W, Hees JJ, Brink D, Muller-Sebert W, Kriele A, Williams OA, Nebel CE. Anisotropic etching of diamond by molten Ni particles. *Appl Phys Lett.* 2010;97(2010):17–20. doi:10.1063/1.3480602.
32. Nebel CE, Rezek B, Shin D, Watanabe H. Surface electronic properties of H-terminated diamond in contact with adsorbates and electrolytes. *Phys Status Solidi Appl Mater Sci.* 2006;203(13):3273–3298. doi:10.1002/pssa.200671401.
33. Oliveira C a. GS, Stein MF, Saito E, Zanin H, Vieira LS, Raniero L, Trava-Airoldi VJ, Lobo AO, Marciano FR. Effect of gold oxide incorporation on electrochemical corrosion resistance of diamond-like carbon. *Diam Relat Mater.* 2015;53:40–44. doi:10.1016/j.diamond.2015.01.009.
34. Ramos BC, Saito E, Trava-Airoldi VJ, Lobo a. O, Marciano FR. Diamond-like carbon electrochemical corrosion resistance by addition of nanocrystalline diamond particles for biomedical applications. *Surf*

- Coatings Technol.* 2014;259:732–736. doi:10.1016/j.surfcoat.2014.09.066.
35. Nart FC, Iwasita T. On the adsorption of sulfate species on polycrystalline platinum An FTIR study in fluoride base electrolyte. *J. Electroanal. Chem.* 1991;308:277–293.
  36. Antolini E. Palladium in fuel cell catalysis. *Energy Environ Sci.* 2009;2:915. doi:10.1039/b820837a.
  37. Feng L, Sun X, Liu C, Xing W. Poisoning effect diminished on a novel PdHoOx/C catalyst for the electrooxidation of formic acid. *Chem Commun.* 2012;48:419. doi:10.1039/c1cc16522d.
  38. Antolini E, Gonzalez ER. Alkaline direct alcohol fuel cells. *J Power Sources.* 2010;195(11):3431–3450. doi:10.1016/j.jpowsour.2009.11.145.
  39. Shao M. Palladium-based electrocatalysts for hydrogen oxidation and oxygen reduction reactions. *J Power Sources.* 2011;196(5):2433–2444. doi:10.1016/j.jpowsour.2010.10.093.
  40. Ravi Krishna E, Muralidhar Reddy P, Sarangapani M, Hanmanthu G, Geeta B, Shoba Rani K, Ravinder V. Synthesis of N4 donor macrocyclic Schiff base ligands and their Ru (II), Pd (II), Pt (II) metal complexes for biological studies and catalytic oxidation of didanosine in pharmaceuticals. *Spectrochim Acta - Part A Mol Biomol Spectrosc.* 2012;97:189–196. doi:10.1016/j.saa.2012.05.073.
  41. Lu J, Zhang H, Chen X, Liu H, Jiang Y, Fu H. Palladium-catalyzed synthesis of aromatic ketones and isoindolobenzimidazoles via selective aromatic C-H bond acylation. *Adv Synth Catal.* 2013;355:529–536. doi:10.1002/adsc.201200743.
  42. Wu XF, Neumann H, Beller M. Palladium-catalyzed oxidative carbonylation reactions. *ChemSusChem.* 2013;6:229–241. doi:10.1002/cssc.201200683.
  43. Chang CM, Hon MH, Leu IC. Outstanding H<sub>2</sub> sensing performance of Pd nanoparticle-decorated ZnO nanorod arrays and the temperature-dependent sensing mechanisms. *ACS Appl Mater Interfaces.* 2013;5:135–143. doi:10.1021/am302294v.
  44. Kalidindi SB, Oh H, Hirscher M, Esken D, Wiktor C, Turner S, Van Tendeloo G, Fisher RA. Metal@COFs: Covalent organic frameworks as templates for pd nanoparticles and hydrogen storage properties of Pd@COF-102 hybrid material. *Chem - A Eur J.* 2012;18:10848–10856. doi:10.1002/chem.201201340.
  45. Ksar F, Sharma GK, Audonnet F, Beaunier P, Remita H. Palladium urchin-like nanostructures and their H<sub>2</sub> sorption properties. *Nanotechnology.* 2011;22:305609. doi:10.1088/0957-4484/22/30/305609.
  46. [www.casaxps.com](http://www.casaxps.com).
  47. Taylor RI. *Phys. Rev. Lett.* 1972;29(16):1088–1092.
  48. Ding L-X, Wang A-L, Ou Y-N, Li Q, Guo R, Xia Zhao W, Xiang Tong Y, Ren-Li G. Hierarchical Pd-Sn alloy nanosheet dendrites: an economical and highly active catalyst for ethanol electrooxidation. *Sci Rep.* 2013;3:1181. doi:10.1038/srep01181.

49. Mavrokefalos CK, Nelson GW, Poll CG, Compton RG, Foord JS. Electrochemical aspects of Pt-Cu and Cu modified boron-doped diamond. *Phys Status Solidi*. 2015;9:n/a–n/a. doi:10.1002/pssa.201532163.
50. Wagner CD, Riggs WM, Davis LE, Moulder JF, Muilenburg GE. Handbook of X-ray Photoelectron Spectroscopy (Perkin-Elmer Co, Minnesota, 1979).
51. Liang ZX, Zhao TS, Xu JB, Zhu LD. Mechanism study of the ethanol oxidation reaction on palladium in alkaline media. *Electrochim Acta*. 2009;54(8):2203–2208. doi:10.1016/j.electacta.2008.10.034.
52. Grdeń M, Czerwiński A. EQCM studies on Pd-Ni alloy oxidation in basic solution. *J Solid State Electrochem*. 2008;12(4):375–385. doi:10.1007/s10008-007-0452-8.
53. Vračar L, Burojević S, Krstajić N. The surface processes at Pd–Ni alloy in acid and alkaline solutions. *Int J Hydrogen Energy*. 1998;23(12):1157–1164. doi:10.1016/S0360-3199(97)00176-6.
54. Jeong M-C. Voltammetric Studies on the Palladium Oxides in Alkaline Media. *J Electrochem Soc*. 1993;140(7):1986. doi:10.1149/1.2220750.
55. Denuault G, Milhano C, Pletcher D. Mesoporous palladium-the surface electrochemistry of palladium in aqueous sodium hydroxide and the cathodic reduction of nitrite. *Phys Chem Chem Phys*. 2005;7(20):3545–3551. doi:10.1039/b508835f.
56. Cai J, Zeng Y, Guo Y. Copper@palladium–copper core–shell nanospheres as a highly effective electrocatalyst for ethanol electro-oxidation in alkaline media. *J Power Sources*. 2014;270:257–261. doi:10.1016/j.jpowsour.2014.07.131.
57. Hu GZ, Nitze F, Jia X, Sharifi T, Barzegar HR, Gracia-Espino E, Wagberg T. Reduction free room temperature synthesis of a durable and efficient Pd/ordered mesoporous carbon composite electrocatalyst for alkaline direct alcohols fuel cell. *RSC Adv*. 2014;4(2):676–682. doi:10.1039/C3RA42652A.
58. Peng C, Hu Y, Liu M, Zheng Y. Hollow raspberry-like PdAg alloy nanospheres: High electrocatalytic activity for ethanol oxidation in alkaline media. *J Power Sources*. 2015;278:69–75. doi:10.1016/j.jpowsour.2014.12.056.
59. Ahmed MS, Jeon S. Synthesis and Electrocatalytic Activity Evaluation of Nanoflower Shaped Ni-Pd on Alcohol Oxidation Reaction. *J Electrochem Soc*. 2014;161(12):F1300–F1306. doi:10.1149/2.1041412jes.
60. Bagchi J, Bhattacharya SK. Electrocatalytic activity of binary Palladium Ruthenium anode catalyst on Ni-support for ethanol alkaline fuel cells. *Transit Met Chem*. 2007;32(1):47–55. doi:10.1007/s11243-006-0127-9.
61. Grden' M, Kotowski J, Czerwinski A. The study of electrochemical palladium behavior using the quartz crystal microbalance. *J Solid State Electrochem*. 2000;4(5):273–278.
62. Prabhuram J, Manoharan R. Effects of incorporation of Cu and Ag in Pd on electrochemical oxidation of methanol in alkaline solution. *J Appl Electrochem*. 1998;28:935–941.

63. Chen M, Wang Z-B, Ding Y, Yin G-P. Investigation of the Pt–Ni–Pb/C ternary alloy catalysts for methanol electrooxidation. *Electrochem commun.* 2008;10(3):443–446. doi:10.1016/j.elecom.2008.01.012.
64. Knudsen J, Nilekar AU, Vang RT, et al. A Cu / Pt Near-Surface Alloy for Water - Gas Shift Catalysis. 2007;(3):3838–3842.